Valence and inner hole responses via the ^{208}Pb$(\vec{d},t)^{207}$Pb reaction at $E_d = 200$ MeV and form factor dependence

H. Langevin-Joliot,[1] J. Van de Wiele,[1] F. Jourdan,[1] J. Guillot,[1] E. Gerlic,[2] L. H. Rosier,[1] A. Willis,[1] C. Djalali,[1,3] M. Morlet,[1] E. Tomasi-Gustafsson,[4] N. Blasi,[5] S. Micheletti,[5] and S. Y. van der Werf[6]

[1]*Institut de Physique Nucléaire, IN2P3-CNRS, BP No. 1-91406 Orsay, France*

[2]*Institut de Physique Nucléaire, IN2P3-CNRS, 43 Bd du 11 Novembre, 69622 Lyon-Villeurbanne, France*

[3]*Department of Physics and Astronomy, University of South Carolina, Columbia, South Carolina 29208*

[4]*DAPNIA-SPhN and Laboratoire National Saturne, CEN-Saclay, F 91191, Gif sur Yvette, France*

[5]*INFN and University of Milan, Physics Department, Via Celoria 16, 20133 Milan, Italy*

[6]*Kernfysisch Versneller Instituut, 9747 AA Groningen, The Netherlands*

(Received 19 May 1998)

The study of the ^{208}Pb$(\vec{d},t)^{207}$Pb reaction at $E_d = 200$ MeV has been extended up to typically $E_x = 40$ MeV in ^{207}Pb using a polarized beam with both vector and tensor components. Two-step pickup reactions involving low multipolarity collective transitions have been evaluated for the first time via systematic coupled channel calculations, allowing a new approach of the background determination. The $(\vec{d},t)$ observables corresponding to the overlapping $1h_{11/2}$, $1g_{7/2}$, and $1g_{9/2}$ inner hole responses have been analyzed up to $E_x = 25$ MeV via a least squares fit procedure. Necessary input values were deduced for hole states of interest from finite range distorted wave (DWBA) calculations. The optical parameters and the range function were those successfully used in a previous survey of valence state observables. The highest j transitions are enhanced in the reaction and analyzing powers exhibit strongly characteristic features for $j_- = l - 1/2$ versus $j_+ = l + 1/2$ states. We have calculated for the first time the separation energy dependence of nlj transition observables, taking into account the form factor modifications induced by the hole coupling with surface vibrations. The calculations have been performed in the framework of the quasiparticle-phonon model (QPM). This analysis (QPMFF) predicts a large variation of differential cross sections with excitation energy of the hole fragments, while angular distribution shapes remain quite stable. The strength distributions resulting of the QPMFF analysis and of a standard analysis using DWBA observables calculated at the centroid energies are systematically compared. As a general rule, the QPMFF analysis increases the strength concentration toward lower excitation energy. The corresponding $1h_{11/2}$, $1g_{7/2}$, and the tentative $1g_{9/2}$ strength distributions are compared and discussed with the available theoretical calculations. In particular, the narrower spreading widths deduced via the QPMFF analysis are quite well predicted by the calculation of spectral functions in a modified mean field. The $1i_{13/2}$ and $1h_{9/2}$ valence strength distributions are revisited along this new approach and found to be in fair agreement with the fragmentation predicted by the QPM, which is not the case of inner hole strength distributions. [S0556-2813(98)04510-5]

PACS number(s): 21.10.Pc, 25.45.Hi, 24.70.+s, 24.10.Eq

I. INTRODUCTION

Experimental investigations and theoretical studies of neutron-hole response functions at high excitation energy have been performed in a rather large number of nuclei [1,2]. Several experiments have focused on the doubly magic ^{208}Pb nucleus, which is a test case for different theoretical approaches [3–9]. Most experimental studies have been performed with unpolarized beams, using the $(^3\mathrm{He},\alpha)$ reaction at several incident energies [10–13]. These experiments have given evidence for a large fragmentation of valence hole strengths and for a concentration of the $1h_{11/2}$ inner strength in a structure around $E_x \sim 8.5$ MeV.

More recent results published by our group [14] have been obtained via the $(\vec{d},t)$ reaction at $E_d = 200$ MeV using a polarized deuteron beam with both vector and tensor components [14]. This reaction combines the advantage of a strong selectivity for the population of high-l hole states with new possibilities of identification of $j_- = l - 1/2$ versus $j_+ = l + 1/2$ states given by characteristic features of both vector and tensor analyzing powers at the above incident energy [15,16]. These properties proved especially useful to achieve an unambiguous identification of the $1i_{13/2}$ and $1h_{9/2}$ high-lying groups. They allowed us to study the $1h_{11/2}$ response function up to $E_x = 14.5$ MeV and to give the first reliable evidence for a concentration of the $1g_{7/2}$ strength around $E_x = 11$ MeV.

It seemed to us interesting to extend the investigation of inner hole states over a larger range of excitation energies than in [14], also using the $(\vec{d},t)$ reaction at $E_d = 200$ MeV. A new investigation of the ^{208}Pb$(\vec{d},t)$ reaction has been performed up to $E_x \sim 40$ MeV and at selected angles to complement the previous data. The present paper reports on the $1h_{11/2}$, $1g_{7/2}$, and $1g_{9/2}$ strength distributions up to $E_x = 25$ MeV, and revisits the $1i_{13/2}$ and $1h_{9/2}$ valence strengths.

We emphasize the following point, of major importance, which motivates the new approach used in the data analyses. Results of distorted-wave Born approximation (DWBA) calculations, here finite range calculations, are well known to

depend sensitively on the hole form factors. It has already been pointed out in Ref. [14] that the well depth procedure generally used in the calculation of form factors was questionable for hole fragments spread over a large excitation energy range. The form factors were instead calculated in a core potential of constant depth complemented by an empirical surface-peaked potential adjusted to reproduce the binding energies. A systematic investigation of the separation energy dependence of hole form factors in ^{207}Pb has recently been performed in the framework of the quasiparticle phonon model. These calculations, which include explicitly the hole coupling with surface vibrations mainly responsible for the hole fragmentation, point to a quite significant increase of form factor radii [17]. This new approach is used in the present work to calculate form factors, allowing an analysis of the data consistent with current assumptions on the fragmentation process. It supersedes the empirical attempt of Ref. [14]. Valence and inner hole responses deduced via this new analysis are systematically compared with those deduced assuming no dependence of DWBA observables with excitation energy for transitions of the same nlj.

It is well known that determinations of single hole response functions at high excitation energy are hampered by uncertainties on the contributions of multistep reactions to the experimental spectra. We present in this paper an evaluation of two-step pickup contributions performed via coupled channel calculations, allowing a new approach of the background estimation.

The paper is organized as follows. The experimental procedure and the raw data are presented in Sec. II. The evaluation of two-step pickup observables is described in Sec. III. The excitation energy dependence of DWBA observables calculated for each hole state is discussed in Sec. IV. Section V presents the data analysis in the continuum region. Fragmentation and spreading deduced for valence and inner hole states are compared in Sec. VI with theoretical calculations. Section VII summarizes the results and conclusions.

II. EXPERIMENTAL PROCEDURE AND OVERALL FEATURES OF THE DATA

The experiment was performed with the polarized deuteron beam available at the Laboratoire National Saturne (LNS). Deuterons polarized in four different states called 5, 6, 7, and 8 [18], which are linear combinations of vector and tensor polarization states, were accelerated sequentially in successive bursts. The outgoing particles labeled with the corresponding deuteron polarized state were analyzed by the high resolution spectrometer SPES1 working in the dispersion matching mode. The vector and tensor polarization parameters, periodically measured with the low-energy $D(\vec{d},p)^3H$ polarimeter [18], reached 92% and 90.5% of the corresponding maximum values. They were found to be very stable within 2% and 1%, respectively. The polarimeter absolute calibration may account for 5% systematic errors in the deduced analyzing powers.

The trajectory positions and angles at the focal plane were measured with the first three localization chambers of the polarimeter ''POMME'' [19], instead of the standard detection previously used in [14]. Energy loss and time of flight measured with the POMME trigger allowed a selection of the tritons of interest among a background of scattered deuterons scattered at 3° and at the highest excitation energies. The ^{208}Pb-enriched (99%) target was 39 mg/cm^2 thick, and the energy resolution achieved for the tritons was 200 keV. The horizontal and vertical angular acceptances were set, respectively, at 2° and 4° and achieved partly with software cuts.

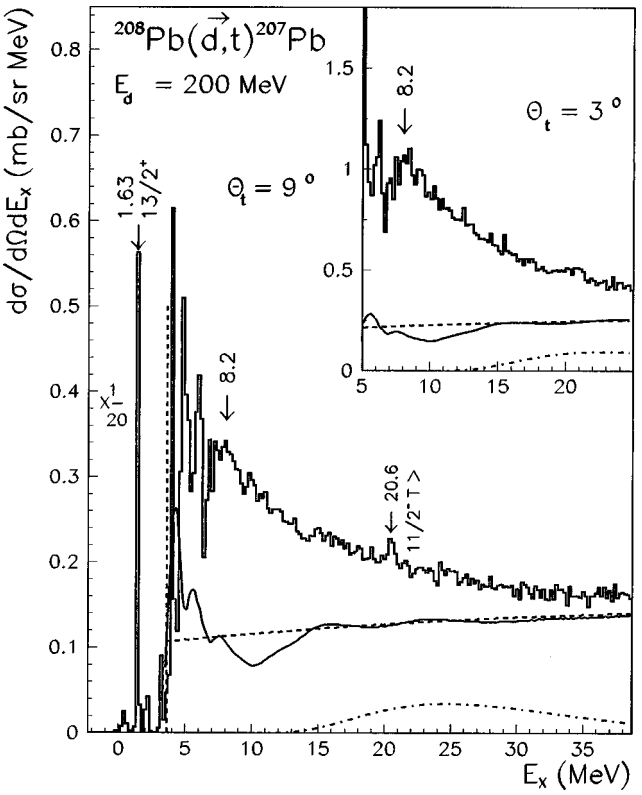

FIG. 1. Excitation energy spectra of the residual nucleus ^{207}Pb compressed in 200 keV energy bins. The solid and dashed lines are estimated contributions of the background referred to as back1 and back2, respectively (see Sec. V C 2). The dot-dashed line is the contribution of hole transitions deeper than $1g_{9/2}$.

The measurements were performed at selected angles and field settings in order to complement up to 15° and $E_x \sim 31$ MeV the data obtained in the previous experiment in the region of inner hole states. The background behavior was further studied at field settings centered around $E_x = 35$ MeV at 3° and 9° and around $E_x = 43$ MeV at 6°, 9°, 12°, and 15°.

Two beam monitors, described in [15,16], were used. The ratio of the two monitor information was found to be stable within less than 10% (generally 5%). An uncertainty of 10% on cross sections at each angle (or the statistical errors if larger) has been conservatively adopted. The absolute calibrations, performed by the carbon activation method used at the LNS [20], may induce a systematic error of typically $\sim$15% on absolute cross sections. We have renormalized by a factor of 1.2 the data of our previous experiment [14] for consistency, as already done in [16] for the valence level results. The renormalized data have been combined with those of the present experiment to get the ^{207}Pb residual spectra discussed in the following.

Excitation energy spectra taken at 9° and 3°, compressed in 200 keV energy bins, are presented in Fig. 1. ^{11}C and ^{15}O

TABLE I. Characteristics of dipole, quadrupole, and octupole excitations used in coupled channel calculations.

	E_x (MeV)	β	Width (MeV)	Ref.
GDR	13.7	0.187	4.0	[21, 22]
2^+	4.086	0.051	-	[22]
GQR	10.7	0.084	2.6	[23]
3^-	2.61	0.116	-	[22]
LEOR[a]	6.1	0.065	4.7–7.5	[24]
HEOR[b]	19.5	0.067	7.0	[21]

[a]The concentration of 3^- discrete levels around 6.1 MeV is referred to as LEOR in the text.
[b]Estimations.

impurity peaks have been subtracted out with the help of CH2 and Mylar target measurements. The main feature of these spectra beyond the valence region is the structure around $E_x = 8.2$ MeV attributed to the $1h_{11/2}$ strength [1,14]. No indication for a bump which could be attributed to the $1g_{7/2}$ or $1g_{9/2}$ strength in ^{207}Pb is observed. The highest part the spectra are dominated by multistep reactions, as discussed later on.

III. TWO-STEP $(\vec{d},t)$ REACTION AT $E_d = 200$ MeV

A. Configurations and general method

A realistic calculation of two-step pickup spectra based on a complete description of all possible inelastic and neutron pickup transitions is out of range. One may, however, anticipate that low-multipolarity collective transitions would play a major role in building two-step $(\vec{d},t)$ spectra at forward angles and not too large excitation energies. This assumption is strongly suggested by the well-known features of ^{208}Pb inelastic spectra induced by medium-energy particles. In particular the first 2^+ and 3^- collective levels and the giant quadrupole resonance are strongly excited.

We have investigated the two step $(\vec{d},t)$ contributions involving quadrupole, octupole, and or Coulomb-excited dipole transitions, and all valence or inner hole pickup transitions. Such two-step reactions populate multiplets of states belonging to numerous one-quasihole–one-phonon ($|1qh \otimes 1ph\rangle$) configurations. The following procedure was adopted to obtain the corresponding two-step cross sections and analyzing powers as function of excitation energy. Coupled channel calculations were first performed, neglecting both the hole and phonon spreading. Summed cross sections over all states of each multiplet and the corresponding averaged analyzing powers were then calculated. The estimated spreading of the different configurations was taken into account at the final stage of the calculations, as explained in Sec. III C.

The excitation energies and β values of the phonon excitations used in coupled channel calculations are summarized in Table I. The well-known energies of the first levels in ^{207}Pb have been used for pickup transitions in the valence shell. For inner hole transitions, Hartree-Fock energies calculated with the Skyrme III force [25] have been shifted down by 2 MeV, taking into account the predictions of Ref. [7]. It should be noticed that interferences between one-step and two-step amplitudes, or two-step amplitudes built on different configurations, are not taken into account in the present coupled channel calculations. This approximation is well justified for cross sections summed over a significant energy interval, and more questionable for analyzing powers.

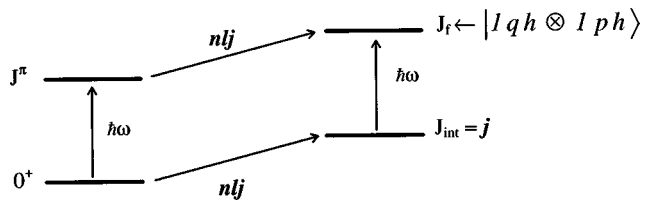

FIG. 2. Two-step pickup amplitudes.

B. Coupled channel calculations

We have performed systematic calculations of two-step cross sections and analyzing powers, taking into account coherently the two amplitudes involving inelastic transitions in the deuteron and triton channels, as shown in Fig. 2.

The two-step pickup observables have been calculated within the zero-range approximation (hereafter ZR) using the coupled channel code CCZR [26] with the deuteron and triton potential parameters D200ZR and T200ZR given in Ref. [15]. Such calculations will be referred to as CCZR. ZR DWBA calculations of the one-step $(\vec{d},t)$ reaction performed with these potentials have been shown [15] to describe rather well valence level cross sections (using a normalization factor $N = 1.7$ instead of the standard value $N = 3.3$) and, to a lesser extent, vector analyzing powers. The strongly negative tensor analyzing powers measured at small angles for the $9/2^-$ level (with $j_- = l - 1/2$) are not at all reproduced, which is not surprising as this effect has been shown in [15,16] to result from S and D interference terms induced by the range function.

It seems to us interesting to compare CCZR cross sections summed over all levels of a given multiplet and averaged analyzing powers, with ZR DWBA observables calculated for the hole transition involved in the multiplet configuration. Examples of such comparisons are given in Fig. 3 for important configurations. Two-step cross sections are found rather small, with angular distribution slopes less steep than for direct pickup, as expected. On the other hand, the calculated two-step and one-step analyzing powers exhibit fairly similar features. The same qualitative conclusion also applies for other configurations.

Under these conditions, a reasonable assumption is that the corrections needed to better reproduce one-step analyzing powers starting with ZR DWBA predictions would also improve two-step analyzing powers deduced of CCZR calculations for configurations built on the same pickup transitions. Such additive corrections have been determined using the valence level data. The quite similar shapes of the observable angular distributions calculated for transitions with different l values but with the same number of nodes and the same spin and angular momentum coupling [15,16] allow using these corrections for configurations involving inner hole states. Extrapolating the conclusions concerning the one-step reaction corrected for the new calibration and valence level

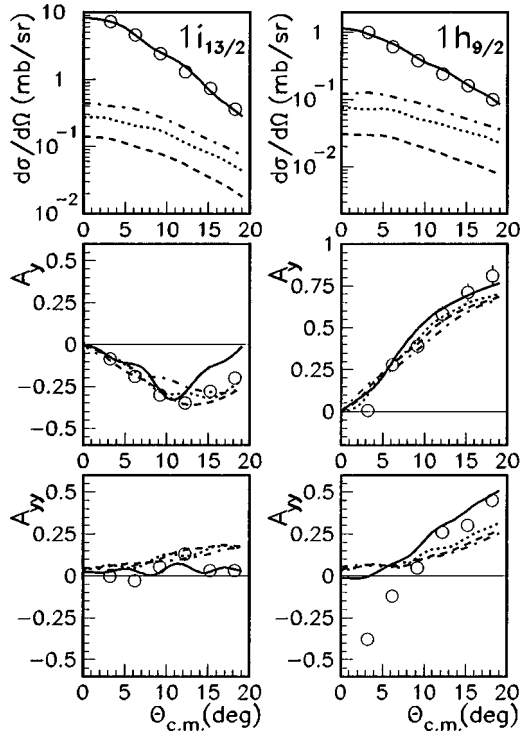

FIG. 3. Angular distributions of one-step and two-step pickup observables involving $1i_{13/2}$ (left) and $1h_{9/2}$ (right) pickup transitions. Solid lines: one-step pickup transitions to the 1.63 MeV and 3.42 MeV first valence levels. ZR DWBA cross sections are normalized to the experimental data. Dashed lines: two-step pickup populating configurations involving the 2^+ transition at $E_x = 4.086$ MeV. Dotted lines: two-step pickup populating configurations involving the giant quadrupole resonance. Dash-dotted lines: two-step pickup transitions involving the 3^- transition at $E_x = 2.61$ MeV.

analysis, a normalization factor of $N = 1.85$ was adopted in CCZR calculations.

C. Two-step excitation energy spectra

Each $|1qh \otimes 1ph\rangle$ configuration generates a number of levels spread over a range of excitation energies in the residual nucleus. The spreading of most configurations has been described by Lorentzian-type distributions. The adopted low-energy side and high-energy side widths of these distributions have been chosen to take qualitatively into account estimated widths of hole strength distributions together with known or estimated widths for the excitation involved in the configuration (see Table I). For the configurations involving a valence hole coupled to the low-energy 2^+ and 3^- excitations, we have considered separately the groups of levels associated with the quasihole levels and the groups associated with residual valence strengths in higher-lying fragments. The distributions in excitation energy of both kinds of groups have been smoothed out with simple trapezoidal shapes.

The predicted two-step $(\vec{d},t)$ spectrum at 9° summed over quadrupole, octupole, and Coulomb-excited dipole contributions is shown in Fig. 4 together with separated 2^+, 3^-, and 1^- contributions. The procedure used to get such spectra involves rather large uncertainties, so that detailed features

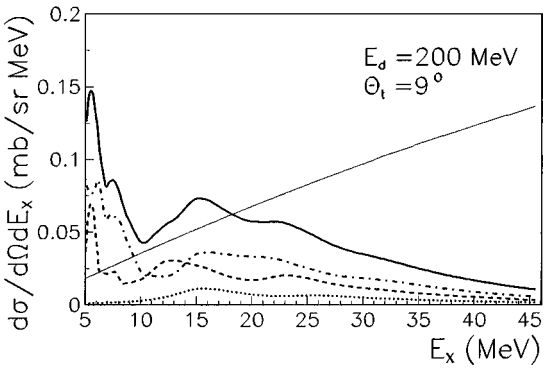

FIG. 4. Components of background back1 at 9°. Thick solid line: calculated two-step spectrum back1a. Dotted line: contribution of the GDR to back1a. Dashed line: contribution of quadrupole transitions to back1a. Dash-dotted line: contribution of octupole transitions to back1a. Thin solid line: semiempirical component back1b (see Sec. V C).

predicted in the valence region are not significant.

A first remark bears on the cross sections predicted around $E_x = 6$ MeV. The present results point to the conclusion that the background of indirect pickup does not drop to zero at such excitation energy, as assumed previously [14]. In the region of interest for the analysis of the first inner hole states, the main contributions come from the valence⊗LEOR configurations, and to a smaller degree from the valence⊗QGR configurations (see Table I). Beyond ~25 MeV, the two-step spectra built for each multipolarity decrease as function of excitation energy.

IV. EXCITATION ENERGY DEPENDENCE OF $(\vec{d},t)$ OBSERVABLES

A special point of interest for DWBA analyses is the dependence of form factors on separation energy of strength fragments belonging to a given hole state. The well depth procedure generally used for analyzing low-lying levels is not well suited for describing fragments several MeV away from the quasihole energy, as discussed in [14]. Instead, it has been suggested that the coupling with surface vibrations, if responsible for the fragmentation process, would better be taken into account through a modification of the effective potential well radius. More precisely, it has been pointed out by Austern [27] that the coupling with surface vibrations induces a surface-peaked source term in the inhomogeneous equation describing admixed wave functions. It has also been noticed that modifications of form factor shapes only depend on the source term shape, and that such a shape could be approached via a structure calculation without solving a complex set of coupled equations.

Along these lines, form factors of neutron and proton hole states in the valence and inner shell of ^{208}Pb have recently been studied within the quasiparticle-phonon model (QPM) [17]. The important conclusion is that the overall behavior of the calculated form factors as a function of separation energy can be described using a mean source term localized about 4.5% inside of the well radius. This source term can be parametrized with a first-derivative Woods-Saxon shape. A quite significant increase of form factor radii with separation

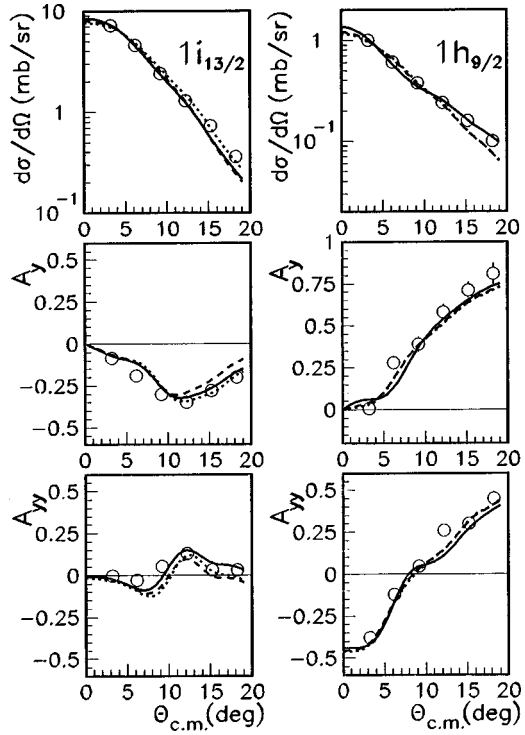

FIG. 5. Angular distribution of $(\vec{d},t)$ observables as function of excitation energy. DWBA cross sections are normalized to experimental values at small angles. Solid lines: quasihole levels. Dashed lines: $E_x=4.7$ and 7.2 MeV, respectively, for $1i_{13/2}$ and $1h_{9/2}$ fragments. Dotted lines: $E_x=8.5$ and 9.2 MeV, respectively, for $1i_{13/2}$ and $1h_{9/2}$ fragments.

energy of fragments of a same high-j hole strength results of such calculations [17].

The parameters of the Woods-Saxon well used in the QPM calculations differ from the parameters of the Woods-Saxon well adopted for the calculation of hole form factors in our previous analyses of the $^{208}\mathrm{Pb}(\vec{d},t)^{207}\mathrm{Pb}$ reaction [14–16]. In order to allow a direct comparison of the results, a new mean source term was calculated with these latter parameters. The source term was fitted with a first-derivative Woods-Saxon shape of radius $r=1.165A^{1/3}$ fm and surface thickness $a=0.54$ fm (compared with $r=1.22A^{1/3}$ fm and $a=0.7$ fm for the binding Woods-Saxon potential). The normalized form factors obtained for each hole state at several excitation energies were then used in finite range DWBA calculations.

The behavior of the observables calculated under these conditions (hereafter QPMFF analysis) at three excitation energies spanning the $1i_{13/2}$ and $1h_{9/2}$ hole fragments is shown in Fig. 5. The angular distribution shapes of σ, A_y, and A_{yy} are found nearly insensitive to excitation energy, within several MeV. However, absolute values of cross sections per picked neutron increase with excitation energy. Similar observations are made in the case of inner hole states. As a result, for a same experimental cross section, the spectroscopic factors of fragments below the reference energy (chosen near the expected strength distribution centroid) are larger than the value calculated with the form factor corresponding to this latter energy, and smaller beyond.

Systematic DWBA calculations have been performed for the different hole states of interest in order to determine the ratio $R_{C^2S}(E_X)$ of spectroscopic factors deduced via the above QPMFF analysis to those obtained via a standard analysis relying on DWBA observables calculated near the centroid energy. In each case, we have considered the range of excitation energies giving stable angular distribution shapes as the one of interest for the fragmentation. Acceptable ranges of excitation energies are typically 2–3 MeV below the centroid energies and several MeV beyond. The largest variations of R_{C^2S} with E_X are obtained for inner hole states, especially the $1g_{7/2}$ state, as shown in Fig. 6.

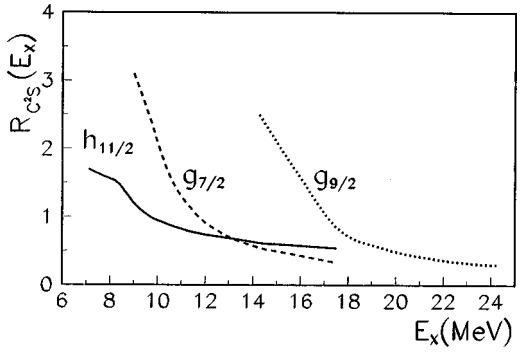

FIG. 6. Ratio $R_{C^2S}(E_X)$ of QPMFF and standard spectroscopic factors for the $1h_{11/2}$, $1g_{7/2}$, and $1g_{9/2}$ inner hole states.

An empirical approach was previously adopted in Ref. [14] in an attempt to take into account the dependence of DWBA observables on excitation energy. In spite of a similar trend than established by the present results, the modifications of spectroscopic factors were quite significantly underestimated.

V. DATA ANALYSIS IN THE CONTINUUM REGION

A. Pickup and background contributions

The experimental spectra beyond $E_x=6.3$ MeV have been divided into excitation energy bins. For each bin, the experimental observables, functions of excitation energy and angle, can be expressed in the continuum as linear sums of pickup contributions from a few inner subshells labeled i, of summed pickup contributions estimated for the deepest shells, and of a physical background, as indicated in Eqs. (1):

$$\sigma^{\mathrm{expt}}=\sum_i C^2S_i\sigma_i^{\mathrm{th}}+\sigma^d+\sigma^b, \tag{1a}$$

$$\sigma^{\mathrm{expt}}A_y^{\mathrm{expt}}=\sum_i C^2S_i\sigma_i^{\mathrm{th}}A_{yi}^{\mathrm{th}}+\sigma^dA_y^d+\sigma^bA_y^b, \tag{1b}$$

$$\sigma^{\mathrm{expt}}A_{yy}^{\mathrm{expt}}=\sum_i C^2S_i\sigma_i^{\mathrm{th}}A_{yyi}^{\mathrm{th}}+\sigma^dA_{yy}^d+\sigma^bA_{yy}^b. \tag{1c}$$

C^2S_i is the spectroscopic strength (i) of a nlj transition in the considered energy bin. σ_i^{th}, A_{yi}^{th}, and A_{yyi}^{th} are theoretical values calculated for the subshell i with the code DWUCK5 [28], using S and D range functions [29] deduced with the supersoft core potential [30] and optical potential parameters given in [16]. σ^d, A_y^d, and A_{yy}^d correspond to summed contributions evaluated for the strongly overlapping subshells deeper than $1g_{9/2}$. σ^b, A_y^b, and A_{yy}^b correspond to the background discussed in Sec. V C.

After subtraction of the background and deep shell contributions, the spectroscopic factors of 2 or 3 different nlj transitions contributing to each energy bin are determined via a least squares fit procedure as in [14].

B. Contribution of the deep-lying shells

The cross sections and analyzing powers of one-step pickup from each filled subshells deeper than $1g_{9/2}$ have been calculated at separation energies shifted down by 2 MeV from separation energies predicted by Hartree-Fock calculations with the Skyrme III force. The results do not change much with this shift suggested by the results of [7].

The contribution of each subshell has been spread in excitation energy assuming a Gaussian-type shape, with parameters $\Gamma_\infty = 25$ and $A = 550$ (see Mahaux and Sartor [8]). Under these conditions the widths of inner hole strength distributions range from ~ 4 MeV for the $1h_{11/2}$ subshell up to 12 MeV for the deepest shells. Significantly narrower widths would induce evident structures in the residual spectra in contradiction with the data, while larger ones do not change significantly the overall results. A typical summed spectra calculated at 9° for the deep shells is shown in Fig. 1. Around $E_x = 25$ MeV, these deep shell cross sections are similar to the summed cross sections shown in Fig. 4 for two-step reactions involving low multipolarity transitions.

C. Contribution of the physical background

The determination of hole strength distributions relies on analyses of one-step pickup spectra. All more complex reactions contribute to the physical background, which must be subtracted out of the experimental data in the excitation energy regions of interest, here $E_x = 6.3$ up to 25 MeV. The methods used for estimating the background have been improved on several points compared with those used in Ref. [14] or more generally in other works [1], introducing more severe constraints. On the one hand, the calculated two-step observables (see Sec. III) have been assumed to dominate the background at low excitation energy. On the other hand, more information on the background angular distributions has been gained from the measurements of three high-excitation-energy bins.

Two estimations of the background, referred to as back1 and back2, have been performed. In the first approach, a background component back1a limited to the two step contributions involving low multipolarities is first calculated. A second component back1b is extrapolated from the high-excitation-energy data corrected for one- and two-step contributions. The background back1 is a sum of the calculated two-step background back1a and of the semiempirical background back1b. In the second approach, the two-step results of Sec. III, are only used to estimate the semiempirical background back2 around $E_x = 5$ MeV, allowing the interpolation up to the high-excitation-energy data corrected for one-step contributions only.

1. Background angular distribution at high excitation energies

The background observables back1b have been obtained for three high-excitation-energy slices in ^{207}Pb by subtracting out the calculated two-step contributions back1a together with the one-step pickup contributions, using Eqs. (1). These

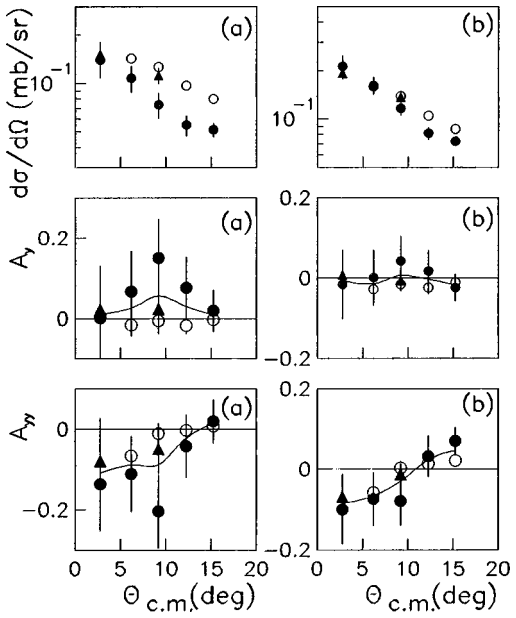

FIG. 7. Angular distributions of background observables for three high-excitation-energy slices. (a) Inner hole and calculated two-step contributions subtracted. (b) Inner hole contributions subtracted. Solid circles: $E_x = 27$ MeV. Solid upper triangles: $E_x = 35$ MeV. Open circles: $E_x = 43$ MeV. Solid line: angular distributions of analyzing powers, averaged over the three excitation energy slices.

latter contributions have been estimated as explained in Sec. V B, with the range of subshells taken into account extended to also include the first inner shell and the $1g_{9/2}$ shell. The background observables back2 have been obtained by subtracting out only the one-step pickup contributions. Angular distributions of background cross sections and analyzing powers are shown in Fig. 7(a) for back1b and Fig. 7(b) for back2. The error bars take into account estimated systematic errors on the subtracted contributions in addition to statistical errors. The angular distributions of back1b and back2 observables exhibit rather similar features.

The cross section angular distributions have smaller slopes than direct pickup ones for each energy slice, with the lowest-excitation-energy slice exhibiting the steepest slope. Vector and tensor analyzing powers exhibit no significant dependence on excitation energy. Mean values were adopted in further analyses. Tensor analyzing powers depend significantly on angles, while vector analyzing powers remain small.

2. Interpolation of the background at intermediate excitation energy

Two-step $(\vec{d},t)$ contributions involving low-multipolarity transitions have been discussed in Sec. III C. The cross sections decrease beyond $E_x = 15$ MeV. Other components of the background are two-step pickup involving multipolarities $L > 3$ and especially three-step and higher-order pickup reactions. Two-step reactions involving high-multipolarity excitations are expected to contribute mainly at larger angles than for low multipolarities, while the contributions of multistep reactions are expected to increase with excitation energy.

The cross section spectra of background back2 or back1b are best estimated at the largest angle of 15° where the calculated one-step and two-step reactions give the smallest relative contribution to the experimental spectra. Linear dependence on excitation energy are adopted for cross section spectra at this angle. The background back2 is parametrized using a mean cross section estimated around $E_x = 5$ MeV for the two-step transitions discussed in Sec. III C and the cross sections deduced for the high-excitation-energy slices. The background back1b is extrapolated from the high excitation energies to zero (see Fig. 4).

As indicated in Sec. V C 1, the slopes of cross section angular distributions decrease toward the highest excitation energies. This variation has been extrapolated linearly in order to estimate the background shapes below 15°. The background spectra back1 and back2 at 9° and 3° are shown in Fig. 1.

VI. RESULTS AND DISCUSSION

The coupling of single particle degree of freedom to the surface modes has been shown to be responsible of major features of strength fragmentation and spreading [1,7,31]. The coupling is generally treated via microscopic calculations. Its overall effect on the strength spreading has also been considered in a phenomenological approach based on dispersion corrections.

Microscopic calculations in the framework of the QPM [5] have allowed systematic comparisons with experimental results bearing on valence and first inner hole states in a number of nuclei [1]. The model contains an averaged field described by a Woods-Saxon well, complemented by pairing interactions and separable multipole and spin-multipole forces. For consistency, the radial shape of the corresponding long-range interaction is taken as the first derivative of the central well. The most complete QPM calculations of neutron hole fragmentation in ^{207}Pb performed by Vdovin [9] allow a systematic comparison with the present results on valence states and inner hole states. $|1qh \otimes 2ph\rangle$ model states are taken into account in addition to $|1qh \otimes 1ph\rangle$ states for the calculations of inner hole states.

Other microscopic calculations in ^{207}Pb, by Bortignon and Broglia [4] and Nguyen Van Giai [3], use the Skyrme III force to calculate Hartree-Fock wave functions and energies. A surface effective interaction of first-derivative Woods-Saxon shape is used in [4]. In [3], the coupling interaction between the hole and the collective excitation is consistently derived from the Skyrme III force. Natural parity collective levels and giant resonances of the core are considered in both calculations performed in the space of $|1qh \otimes 1ph\rangle$ configurations.

The most recent calculations of the $1h_{11/2}$ and $1g_{9/2}$ spectral functions have been performed by Waroquier [32] in the formalism previously used for proton deep hole states [33]. The nucleon-nucleon interaction is described by the Skyrme force SkE2. These calculations differ of Ref. [3] by the description of the core excited states in the space of noninteracting particle-hole configurations, instead of random-phase-approximation- (RPA-) correlated solutions. On the other hand, the iterative method developed to construct a self-consistent solution of the Dyson equation brings in naturally many-body damping effects [34].

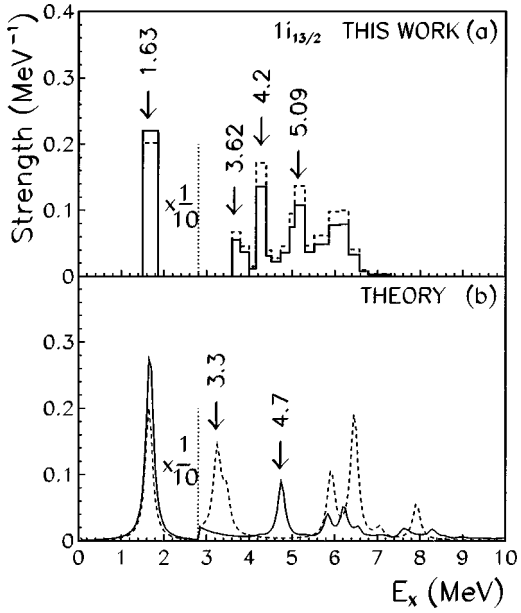

FIG. 8. Experimental and theoretical $1i_{13/2}$ neutron hole strength distributions. (a) Solid line: histogram of the experimental strength deduced with the QPMFF analysis. Dashed line: with the standard analysis. (b) Solid line: results of Vdovin [9]. Dashed line: results of Nguyen Van Giai [3], using the same (0.2 MeV) smearing parameter as Vdovin. The theoretical excitation energy scales have been shifted to reproduce the first level position.

The phenomenological approach of Mahaux and Sartor [7] uses dispersion relations to derive a modified mean field of ^{208}Pb at negative energies, starting with neutron optical potentials at low energy.

The experimental results bearing on the overall $1i_{13/2}$ and $1h_{9/2}$ valence strength distributions and on the $1h_{11/2}$, $1g_{7/2}$, and $1g_{9/2}$ inner hole response functions are presented in the following sections and compared with the theoretical predictions.

A. Valence $1i_{13/2}$ and $1h_{9/2}$ strengths

A detailed description of the $1i_{13/2}$ and $1h_{9/2}$ groups identified via the $(\vec{d},t)$ reaction with 100 keV energy resolution has been discussed in Ref. [14] and compared with previous data [10–13]. The following discussion bears on the overall strength distributions deduced via the new analyses of the same data revised for the monitor calibration. Both analyses differ from those of Ref. [14] through the choice of the supersoft core range function [adopted for consistency with the systematic analysis of the $(\vec{d},t)$ reaction [16]] instead of the Paris range function.

The standard analysis has been performed with DWBA observables calculated at $E_x = 2.2$ MeV and $E_x = 4.2$ MeV for the $1i_{13/2}$ and $1h_{9/2}$ strengths, respectively (instead of the quasihole energies used in [14]). The QPMFF strength distributions taking into account the excitation energy dependence of form factors have been deduced from the standard ones using the ratio $R_{C^2S}(E_X)$ as explained in Sec. IV. The $1i_{13/2}$ and $1h_{9/2}$ strength distributions are shown in Fig. 8 and Fig. 9, respectively, together with theoretical predictions of Refs. [3,9]. The results are summarized in Table II.

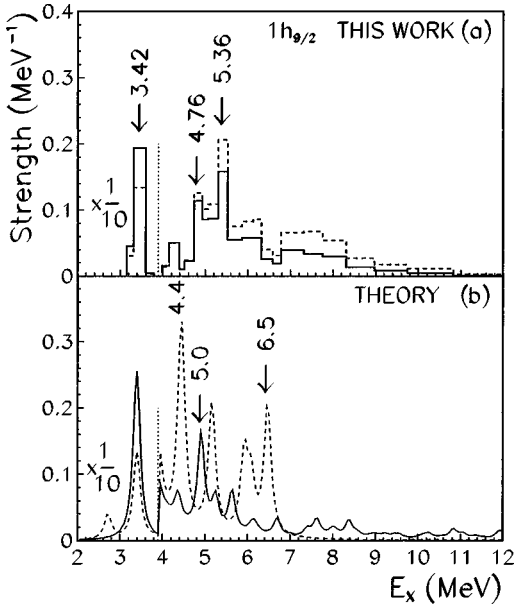

FIG. 9. Experimental and theoretical $1h_{9/2}$ neutron hole strength distributions. (a) and (b) same as for Fig. 8.

The valence strengths concentrated in the quasihole levels are larger with the QPMFF analysis than with the standard one, while the strengths in the high-lying fragments are smaller, as shown in Fig. 8, Fig. 9, and Table II.

As a result, the $1i_{13/2}$ and $1h_{9/2}$ strength centroids are shifted down by ~ 0.2 MeV and ~ 0.5 MeV, respectively. The role of the form factor energy dependence is especially striking in the case of the $1h_{9/2}$ strength, leading to a 45% larger strength in the level at $E_x = 3.42$ MeV, while the fragment-summed strength decreases by nearly 50%. It brings the $1h_{9/2}$ strength distribution in fair agreement with the QPM predictions of Vdovin [9]. The strength exhausted in the quasihole level is fairly reproduced by the calculations of Bortignon and Broglia [4] and Mahaux and Sartor [7] and underestimated by the self-consistent calculations of Nguyen van Giai [3]. The strong fragmentation predicted by these latter calculations (in spite of a smaller number of configurations than in [9]) would point to a too large coupling interaction. The same conclusions apply to the $1i_{13/2}$ strength, to a lesser extent (see Table II).

It is worthwhile to notice that no contribution of two-step pickup reactions has been subtracted out, except for the $1i_{13/2}$ level at $E_x = 4.2$ MeV, as explained in Ref. [14]. Subtracting out the summed two-step cross sections between $E_x = 4.5$ and 7.5 MeV could possibly lead to a $\sim 20\%$ reduction of the $1i_{13/2}$ and $1h_{9/2}$ strengths given in Table II. Such a correction would improve the agreement with the QPM model achieved with the QPMFF analysis. The estimated shifts of the strength centroids remain within error limits.

B. $1h_{11/2}$, $1g_{7/2}$, and $1g_{9/2}$ inner hole strengths

1. Pickup transitions $E_x = 6.3 - 25.5$ MeV

The pickup transitions have been analyzed after subtraction of the background back1 or back2 and of contributions of hole states deeper than $1g_{9/2}$ (see Sec. V). The energy bin widths increase from ~ 0.5 MeV around $E_x = 6.5$ up to 2.5 MeV at high excitation energies. Background corrections

TABLE II. Integral characteristics of the $1i_{13/2}$ (top) and $1h_{9/2}$ (bottom) strength distributions. E_x^{qh} and E_x^c are the quasihole and the centroid excitation energies. Experimental values within ( ) are derived from the standard analysis.

	Quasihole level		Total	
	E_x^{qh} (MeV)	$C^2S/2j+1$	E_x^c (MeV)	$C^2S/2j+1$
This work[a]	1.63	0.79	2.35	0.98
			2.2[b]	0.94[b]
		(0.73)	(2.55)	(0.96)
Theory[c]				
Ref. [9]	0.13	0.91	[1.93]	0.98[d]
Ref. [4]	−0.27	0.78	1.8	0.82[e]
Ref. [7]	0.37	0.71		
Ref. [3]	−1.32	0.64	[2.3]	0.84[d]
This work[f]	3.42	0.63	4.2	0.88
			4.1[b]	0.83[b]
		(0.44)	(4.8)	(0.79)
Theory[c]				
Ref. [9]	0.32	0.76	[3.7]	0.96[g]
Ref. [4]	−0.58	0.60	3.8	0.84[h]
Ref. [7]	0.32	0.77		
Ref. [3]	−1.58	0.43	4.0	0.86[i]

[a]Strength distribution up to $E_x = 7.3$ MeV, assuming a smooth overlap with the $1h_{11/2}$ strength from $E_x = 6.3$ MeV.
[b]With correction for additional background.
[c]Predictions obtained after shifting the energy scales by the values given in column 2 to match the quasihole level to the experimental position.
[d]Up to $E_x = 7.3$ MeV.
[e]Up to $E_x = 6.3$ MeV.
[f]Strength distributions up to $E_x = 11$ MeV assuming a smooth overlap with the $1g_{7/2}$ strength from $E_x = 8.6$ MeV.
[g]Up to $E_x = 11$ MeV.
[h]Up to $E_x = 6$ MeV.
[i]Up to $E_x = 7.2$ MeV.

are typically 10% around $E_x = 10$ MeV and reach $\sim 70\%$ beyond $E_x = 20$ MeV even at the smallest angle. This induces large errors in the pickup data at the highest excitation energies.

Typical angular distributions of the three observables obtained subtracting back1 are shown in Fig. 10. The angular distributions are rather similar for the different energy bins. Vector analyzing powers are systematically negative, as expected for dominant contributions of the $1h_{11/2}$ or $1g_{9/2}$ strengths. Negative values of tensor analyzing powers at 3° are related to $1h_{9/2}$ and $1g_{7/2}$ contributions.

The standard analysis has been performed with DWBA observables calculated at $E_x = 9.7$ MeV, $E_x = 11.7$ MeV, and $E_x = 17$ MeV for the $1h_{11/2}$, $1g_{7/2}$, and $1g_{9/2}$ hole states, respectively. As already noticed, the $(\vec{d},t)$ reaction at $E_d = 200$ MeV allows a very clear identification of $j_- = l - 1/2$ versus $j_+ = l + 1/2$ states with quantum number $n = 1$, but not of orbital l values. Systematic fitting attempts were performed for each energy bin, choosing two or three nlj transitions depending on the energy range. In each attempt, one $j_+ = l + 1/2$ transition $1i_{13/2}$, $1h_{11/2}$, or $1g_{9/2}$, one $j_- = l - 1/2$ transition $1h_{9/2}$ or $1g_{7/2}$, and possibly the group of

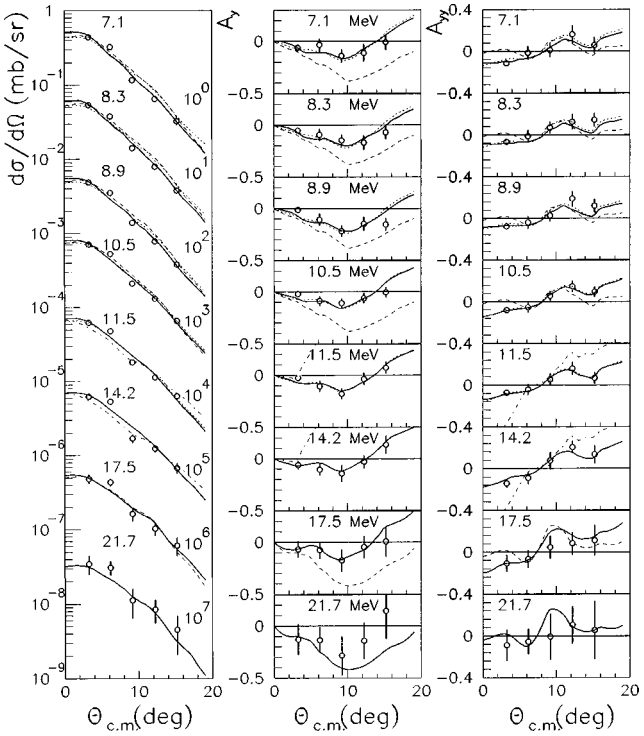

FIG. 10. Typical angular distributions of cross sections and analyzing powers for excitation energy slices between $E_x = 6.3$ and 25.5 MeV. The contributions back1 are subtracted (see Sec. V C). The mean excitation energy of each slice is indicated. Solid lines: best fit angular distributions. Dotted lines: fits obtained with two transitions only (such as $h_{11/2}, g_{7/2}$) where they do not correspond to the best fit. Dashed lines: angular distributions of pure j_+ transitions. Dash-dotted lines: angular distributions of pure j_- transitions.

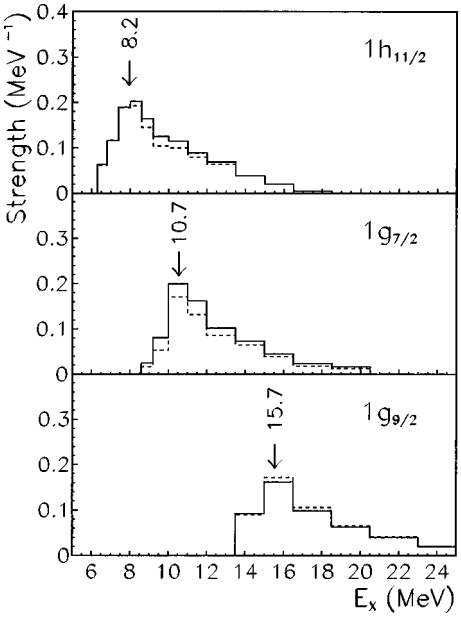

FIG. 11. Dependence of inner hole strength distributions (QPMFF) on the background choice (see Sec. VI). Solid lines: back1 subtracted. Dashed lines: back2 subtracted.

low-l $2d$ and $3s$ transitions were considered. The calculated angular distributions corresponding to the best fits or fits with two transitions only are compared in Fig. 10 with the experimental results. The fits below $E_x = 12$ MeV are improved when the low-l transitions exhausting about 70% of the sum rule are included. Fits of comparable quality are achieved if the background back2 is subtracted out of the data, instead of back1. The QPMFF strength distributions are derived from the standard ones using the ratio $R_{C^2S}(E_X)$ shown in Fig. 6.

The standard strength distributions and the QPMFF ones have been built for the $1h_{11/2}$ and $1g_{7/2}$ states and tentatively for the $1g_{9/2}$ state using the best fit results. Smooth overlaps of the $1i_{13/2}$ and $1h_{11/2}$ strengths, $1h_{9/2}$ and $1g_{7/2}$ strengths, and $1h_{11/2}$ and $1g_{9/2}$ strengths (see Sec. IV) have been assumed.

The sensitivity of strength distributions to the background choice back1 or back2 is illustrated in Fig. 11. The differences are generally within errors bars. The largest effects are observed for the $1g_{7/2}$ strength which is mostly concentrated in the excitation energy region where the shapes of back1 and back2 differ significantly.

The $1h_{11/2}$, $1g_{7/2}$, and $1g_{9/2}$ experimental and theoretical strength distributions are shown in Figs. 12, 13, and 14, respectively. The main characteristics of the inner hole response functions are the quasihole and the centroid excitation energies, the summed strengths, and the spreading widths. Experimental values deduced with the QPMFF and standard analyses are compared in Table III with the theoretical predictions of Refs. [9, 3, 7, 32].

2. $1h_{11/2}$ strength

The strength distribution deduced with the standard analysis is rather flat around $E_x = 9$ MeV. The maximum noticed in Ref. [14] is here smoothed by the subtraction of previously neglected two-step pickup contributions. The QPMFF strength distribution is narrower, with a rather pronounced peak at $E_x = 8.2$ MeV. For both analyses, the strength summed up to $E_x = 18.5$ MeV achieves $\sim 95\%$ of the sum rule. It would decrease by $\sim 7\%$ if subtracting back2 instead of back1 from the data. The experimental summed strengths compare fairly well with the theoretical predictions, taking into account the different strength distribution shapes.

The strength histograms have been fitted with Gaussian-type curves, along the line adopted for proton deep hole states [7,35] in order to determine the quasihole energies and the spreading widths. As shown in Table III, the quasihole and the centroid excitation energies deduced in the QPMFF analysis are shifted down by 1 MeV and ~ 0.9 MeV from those deduced in the standard analysis. As a result, the agreement of the quasihole energy with the prediction of the QPM model is improved. Apart from the shift of the quasihole energy, the most striking effect of the form factor energy dependence bears on the strength distribution shape described by a strongly reduced spreading width (see Fig. 12).

The QPMFF spreading width remains much too large compared with the calculation of Vdovin [9] including $|1qh \otimes 2ph\rangle$ in the model space [see Table III and Fig. 12(b)]. The fair agreement achieved with the valence results by the QPM calculations (see Sec. VI A) let us think that the coupling built from schematic forces used in the model, even if somewhat too small, cannot explain the above discrepancy. Additional technical limitations are involved in QPM calculations of inner states, such as the too small number of

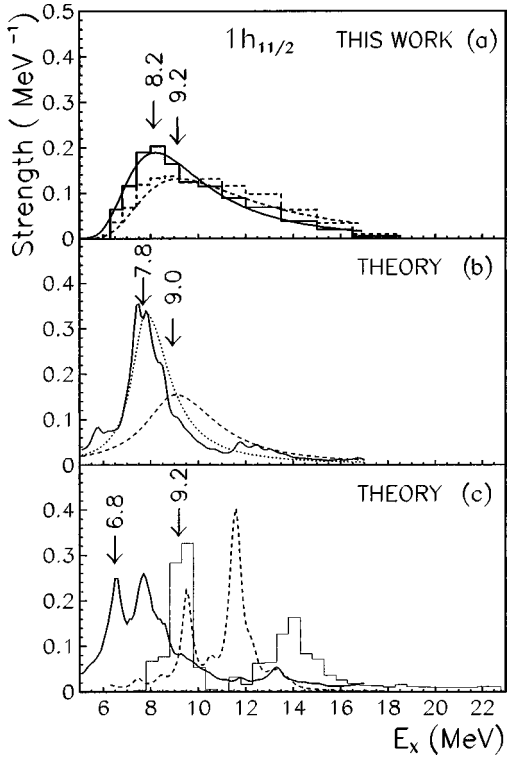

FIG. 12. Experimental and theoretical $1h_{11/2}$ neutron hole strength. (a) Solid lines: histogram of the experimental strength and Gaussian-type fit deduced resulting of the QPMFF analysis. Dashed lines: histogram of experimental data and fit obtained with the standard analysis. (b) Solid line: QPM calculation with $|1qh\otimes 1ph\rangle$ and $|1qh\otimes 2ph\rangle$ components [9]. Dotted line: fit of these results with a Lorentzian shape. Dashed line: modified mean field calculations [7]. (c) Solid line: QPM calculation with $|1qh\otimes 1ph\rangle$ components [9]. Dashed line: calculation of Nguyen Van Giai [3], using the same (0.5 MeV) smearing parameter as Vdovin [9]. Histogram: calculation of Waroquier [32].

$|1qh\otimes 1ph\rangle$ model states imposed by the number of $|1qh\otimes 2ph\rangle$ states to be taken into account and additional cuts of small coupling matrix elements. These limitations may be partly responsible of the too small predicted spreading. The

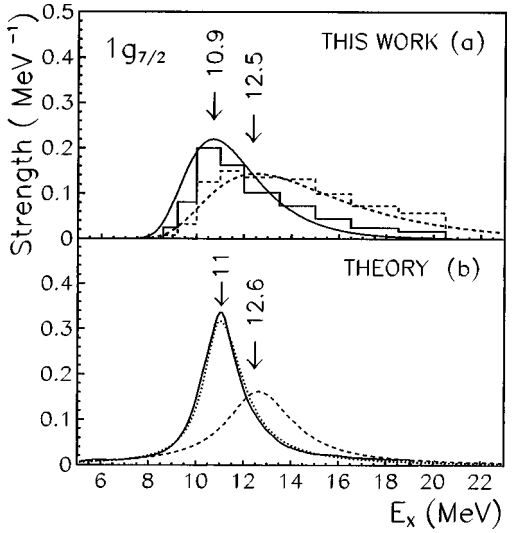

FIG. 13. Experimental and theoretical $1g_{7/2}$ neutron hole strength. (a) and (b) Same as Fig. 12.

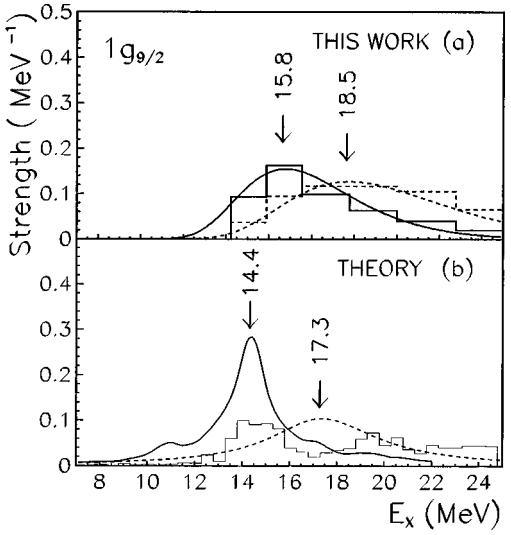

FIG. 14. Experimental and theoretical $1g_{9/2}$ neutron hole strength. (a) Same as Fig. 12. (b) Solid line: QPM calculation with $|1qh\otimes 1ph\rangle$ and $|1qh\otimes 2ph\rangle$ components [9]. Dashed line: modified mean field calculations [7]. Histogram: calculation of Waroquier [32].

missing contributions together with those of higher-order configurations are clearly not correctly simulated by the smearing parameter set to 0.5 MeV.

The spreading width of the QPMFF strength distribution is well predicted by the calculations of Mahaux and Sartor [7] based on dispersion corrections to the mean field. The asymmetric shape of the experimental strength distribution is, however, not well described by the Lorentzian-type shape given in [7].

As shown in Fig. 12(c), the strength distributions calculated by Vdovin [9] and Nguyen van Giai [3] with only $|1qh\otimes 1ph\rangle$ components exhibit two rather pronounced peaks in contradiction with the data. Additional damping is clearly needed, as expected for calculations neglecting any coupling of the hole with higher-order configurations. Less than 10% strengths are predicted at lower excitation energy. High-lying configurations are not included in the calculation of Ref. [3]. The theoretical energy scales of Ref. [9] and Ref. [3] must be shifted by 1.4 MeV and -1.4 MeV, respectively, for matching the first-peak energy to the experimental bump position. The second peak would partly be account for by the coupling of the hole with the $|2d_{5/2}\otimes 3_1^-\rangle$ configuration.

The strength distribution given by Waroquier [32] is characterized by two pronounced peaks shown in Fig. 12(c) and a tail extending smoothly beyond $E_x=23$ MeV up to $E_x \sim 75$ MeV. The first peak is nearly predicted at the same position than in Ref. [3] which calculations use the force Skyrme SIII instead of SkE2. The effect of including RPA correlations may shift the second peak toward lower excitation energy. It would probably not solve the problem of insufficient damping.

3. $1g_{7/2}$ strength

The strength calculated in Refs. [9, 7] are distributed in slightly asymmetric peaks. The smoothing parameter used in Ref. [9] to simulate damping effect in the strength distribution is set at 1 MeV.

TABLE III. Integral characteristics of the $1h_{11/2}$ (top), $1g_{7/2}$ (intermediate), and $1g_{9/2}$ (bottom) strength distributions. $E_x^{\min}$ and $E_x^{\max}$ are the excitation energy limits. $E_x^{\rm qh}$, E_x^c, and $\Gamma\downarrow$ are the quasihole excitation energy, the centroid energy, and the spreading width. Experimental values within parentheses are derived from the standard analysis.

	$E_x^{\min}$ (MeV)	$E_x^{\max}$ (MeV)	$E_x^{\rm qha}$ (MeV)	E_x^c (MeV)	$C^2S/2j+1$	$\Gamma\downarrow$[a] (MeV)
This work[b]	6.3	18.5	8.2	10.0	0.94	3.8
			(9.2)	(10.9)	(0.95)	(5.2)
Theory						
Ref. [9]	6.3	17.0	7.8	8.95	0.82	1.9
Ref. [7]	6.3	18.5	9.03	10.2	0.70	3.66
Ref. [3]	6.3	15.5	[9.6,11.7]	11.1	0.65	[3.7]
Ref. [32]	6.3	17.0	[9.2,13.8]	11.3	0.78	[6.5]
This work[c]	8.6	20.5	10.9	12.6	0.86	3.7
			10.5[d]	12.4[d]	0.78[d]	
			(12.5)	(14.2)	(1.12)	(6.2)
Theory						
Ref. [9]	8.6	19.0	11.0	11.75	0.87	2.0
Ref. [7]	8.6	20.5	12.63	13.15	0.71	3.42
This work[e]	13.5	25.5	15.8	17.7	0.85	5.5
			(18.5)	(19.6)	(1.1)	(7.7)
Theory						
Ref. [9]	13.5	22.0	14.4	15.3	0.63	3.3
Ref. [7]	13.5	25.5	17.33	18.2	0.64	5.51
Ref. [32]	13.5	25.5	[14.5,19.5]	18.2	0.66	[9.4]

[a]Experimental quasihole energies and spreading widths correspond to the Gaussian-type fits shown in Figs. 11, 12, and 13. The theoretical values given for Ref. [9] correspond to Lorentzian type fits. The values within square brackets are the main peak energies and the Gaussian widths derived from the variances σ.

[b]Assuming a smooth overlap with the $1i_{13/2}$ strength from $E_x = 6.3$ to 7.3 MeV.

[c]Assuming a smooth overlap with the $1h_{9/2}$ strength from $E_x = 8.6$ to 11.0 MeV

[d]With back2 instead of back1 subtracted (see text).

[e]Assuming a smooth overlap with the $1h_{11/2}$ strength from $E_x = 13.5$ to 18.5 MeV.

Up to $E_x = 14.5$ MeV, the results obtained with the standard analysis compare rather well with those obtained in Ref. [14] without empirical form factor corrections. The strength distribution then decreases slowly toward high excitation energies. The experimental histogram corresponding to the QPMFF analysis exhibits a pronounced peak of asymmetric shape. The summed strength up to $E_x = 20.5$ MeV is significantly larger in the standard than in the QPMFF analysis where it is found to achieve $\sim$86% of the sum rule (78% if subtracting back2). These latter values compare fairly well with the theoretical predictions within experimental errors.

The quasihole energies and spreading widths deduced via the Gaussian-type fits for the two strength distributions differ quite significantly (see Table III). The quasihole and centroid energies are shifted down by 1.6 MeV in the QPMFF analysis, in better agreement with the QPM predictions.

As for the $1h_{11/2}$ strength, a strong reduction of the spreading width is induced by the form factor energy dependence taken into account in the QPMFF analysis. The spreading width remains, however, much larger than predicted in the QPM model, while it is reproduce within 10% by the mean field calculation (see Table III). The overall shape is, however, much more asymmetric than predicted and does not exhibit wings at low and very high excitation energies.

4. $1g_{9/2}$ strength

A significant part of the $1g_{9/2}$ strength is identified for the first time in the present experiment, in spite of large uncertainties especially below $E_x = 15$ MeV (due to the overlap with the $1h_{11/2}$ strength) and beyond $E_x = 20$ MeV (due to the background subtraction). The summed strength deduced in the QPMFF analysis is estimated to $\sim$85% of the sum rule. As for the other inner hole states, it is possible to achieve reasonable Gaussian-type fits of the strength distributions. The quasihole energy is strongly reduced (by 2.7 MeV) in the QPMFF analysis, as well as the spreading width.

The QPM calculations, performed with a smoothing parameter set to 1 MeV, predict a rather strong concentration of the strength in a peak at $E_x = 14.4$ MeV significantly lower than the position of the experimental maximum deduced with either analyses.

The strength per MeV and the position of the maximum are better accounted for in the mean field calculation [7]. The spreading width as obtained in the QPMFF analysis is in good agreement with the predicted value, in accordance with the $1h_{11/2}$ and $1g_{7/2}$ results.

The strength distribution given by Waroquier calculations [32] exhibits a main peak around $E_x = 14.5$ MeV followed by secondary peaks and a tail extending up to $E_x = \sim 75$ MeV. In spite of giving too much structure, the calculation reproduces fairly well the experimental centroid energy. The maximum strength per MeV is somewhat low, nearer to the result deduced from the standard analysis. The three main groups obtained between $E_x \sim 15$ and 35 MeV at the first step of the iteration procedure are efficiently spread and compressed toward lower excitation energies at the second iteration [32]. Smaller changes are induced by additional steps, so that the final result does not show enough damping compared with the experiment.

The experimental strength summed up to $E_x = 25.5$ MeV appears somewhat large compared with all theoretical predictions, as shown in Table III. This effect is, however, well within the large experimental errors.

VII. SUMMARY AND CONCLUSIONS

We have studied the highly excited neutron hole states in ^{207}Pb via the $(\vec{d},t)$ reaction at $E_d = 200$ MeV. The new experimental data up to $E_x \sim 40$ MeV excitation energy have been combined with the data previously obtained for the same reaction up to $E_x \sim 16$ and 26 MeV [14]. The measurement of three observables (differential cross section and vector and tensor analyzing powers) has led to the determination of the highest-j inner hole strength distributions up to $E_x = 25$ MeV.

Special efforts have been made to evaluate the background of multistep reactions and to correct for them. In

particular, the contributions of two-step pickup involving low-multipolarity collective excitations have been estimated for the first time via coupled channel calculations, adopting rather simple approximations. These contributions present a maximum around $E_x = 5$ MeV. In that region it was previously assumed that the background was negligible. A second but smoother maximum is found at $E_x \sim 15$ MeV. The contributions of the other processes are estimated using the results at the highest excitation energies.

We have calculated for the first time the separation energy dependence of hole state observables corresponding to the form factor modifications induced by the coupling of the hole with surface vibrations. The shape of the source term appearing in the inhomogeneous equations describing admixed wave functions has been derived in the framework of the QPM model as explained in [17]. Strength distributions deduced with the above analysis have been systematically compared with those deduced from the standard analysis that assumes no dependence of cross sections with separation energy.

The valence strengths concentrated in the $1i_{13/2}$ and the $1h_{9/2}$ quasihole levels are larger with the QPMFF analysis than with the standard one, while the strengths in the high-lying fragments are smaller. The effect is especially striking for the $1h_{9/2}$ state.

The new $1h_{11/2}$ and $1g_{7/2}$ strength distributions supersede those previously studied up to $E_x = 14.5$ MeV only [14]. Clear evidence for the deeper $1g_{9/2}$ strength around $E_x \sim 16$ MeV is given for the first time. The results confirm the concentration of $\sim 50\%$ of the $1h_{11/2}$ strength in the bump below $E_x = 10.5$ MeV obtained in previous works [10–14]. The strength distributions deduced up to $E_x = 18.5$ MeV exhaust nearly the sum rule with either analysis. Major parts of the respective sum rule are also exhausted by the $1g_{7/2}$ and $1g_{9/2}$ strengths ($\sim 85\%$ with the QPMFF analysis and 30% more with the standard one). The results bring quantitative support to previous indications [10–12] for dominant contributions of the $1g$ strength in the excitation region $E_x = 10-20$ MeV.

The inner state quasihole energies and spreading widths have been deduced from Gaussian-type fits of the strength distributions, along the method used for proton deep hole states [35]. The quasihole energies deduced with the QPMFF analysis are quite significantly shifted downward in comparison with the standard analysis, while the spreading widths drop to $\sim 70\%$ of their standard values.

The experimental strength distributions have been compared with the predictions of different theoretical approaches. The comparisons refer mainly to the experimental strength distributions deduced with the QPMFF analysis. This latter choice, derived from the important role of hole coupling to surface vibrations, may be better justified for valence states and first inner hole states at not too high excitation energies.

The calculations of Vdovin [9] within the QPM model reproduce fairly well the valence $1i_{13/2}$ and $1h_{9/2}$ fragmentation. A slightly larger coupling strength might improve the achieved qualitative agreement. On the other hand, the calculations underestimate quite significantly the experimental spreading in the case of inner hole states. The two peaks predicted by the $|1qh \otimes 1ph\rangle$ calculation of the $1h_{11/2}$ strength distribution merge into one main peak when $|1qh \otimes 2ph\rangle$ components are included, in agreement with the experiment, but the deduced spreading width is twice smaller that observed. The calculated $1g_{7/2}$ and $(1g_{9/2})$ strength distributions also have much too small widths. Technical limitations involved in the calculations performed with $|1qh \otimes 2ph\rangle$ components may be partly responsible for such discrepancies. These limitations and the coupling, not taken into account, to higher-order configurations are not correctly simulated by a smearing parameter independent of excitation energy.

The calculations of van Giai [3] overestimate significantly the $1h_{9/2}$ strength fragmentation. The large strength predicted for a second peak in the $1h_{11/2}$ strength distribution points to a similar conclusion, in spite of intrinsic limitations of calculations including only $|1qh \otimes 1ph\rangle$ components. The results suggest that the coupling interaction derived from the Skyrme SIII force would be too strong.

The agreement of the $1h_{11/2}$, $1g_{7/2}$, and even $(1g_{9/2})$ spreading widths with the predictions of Mahaux and Sartor [7] for a modified mean field is striking. These theoretical strength distributions have, however, Lorentzian-type shapes, whereas the experimental distributions are much better described by Gaussian-type curves.

The calculations of Waroquier [32] are performed with the Skyrme SkE2 force. Many-body damping processes are included via an iteration procedure. Nevertheless, the damping is strongly underestimated in the predicted $1h_{11/2}$ strength distribution and to a lesser extent in the $1g_{9/2}$ strength distribution. Collective effects neglected in these calculations would modify especially the $1h_{11/2}$ strength shape, but it is not expected that they would account for the insufficient damping. The iteration procedure used to include the hole coupling to higher-order configurations appears less efficient than previously observed for calculations of proton deep hole states [33], especially with low l values. It is worthwhile to notice that the calculated $1g_{9/2}$ strength distribution agrees better with the experiment if adopting the standard analysis. This may indicate that the form factor dependence is overestimated at high excitation energy due to an increasing role of noncollective and/or higher-multipolarity transitions not well described as surface vibrations.

One possibility to check the form factor dependence further would be to compare strength distributions obtained via different reactions chosen to be mainly localized at different radii.

ACKNOWLEDGMENTS

We would like to thank Nguyen Van Giai, M. Waroquier, and G. F. Bertsch for helpful discussions and comments. We are indebted to Nguyen Van Giai and A. Vdovin for communication of their detailed results and to M. Waroquier for communication his unpublished calculations. We are very grateful to Y. Bisson, G. Chesneau, and R. Margaria for their efficient support before and during the experiment and to the technical staff of the Laboratoire National Saturne for its assistance. One of the authors (C.D.) was supported by a grant from the U.S. Department of Energy and the National Science Foundation.

[1] S. Galès, Ch. Stoyanov, and A. I. Vdovin, Phys. Rep. **166**, 125 (1988) and references therein.
[2] G. Duhamel *et al.*, Phys. Rev. C **43**, 1116 (1991), and references therein.
[3] Nguyen Van Giai, in *Proceedings of the International Symposium on Highly Exited States in Nuclear Reactions*, edited by H. Ikegami (RCNP, Osaka, Japan, 1980), p. 682; (private communication).
[4] P. F. Bortignon and R. A. Broglia, Nucl. Phys. **A371**, 405 (1981).
[5] V. J. Soloviev, Ch. Stoyanov, and V. V. Voronov, Nucl. Phys. **A399**, 141 (1982).
[6] R. Majumdar, J. Phys. G **13**, 1429 (1987).
[7] C. Mahaux and R. Sartor, Nucl. Phys. **A493**, 157 (1989), and references therein.
[8] C. Mahaux and R. Sartor, Adv. Nucl. Phys. **20**, 1 (1991).
[9] A. I. Vdovin (private communication).
[10] S. Galès, G. M. Crawley, D. Weber, and B. Zwieglinski, Phys. Rev. C **18**, 2475 (1978).
[11] J. Guillot, J. Van de Wiele, H. Langevin-Joliot, E. Gerlic, J. P. Didelez, G. Duhamel, G. Perrin, M. Buenerd, and J. Chauvin, Phys. Rev. C **21**, 879 (1980).
[12] E. Gerlic, J. Kallne, H. Langevin-Joliot, J. Van de Wiele, and G. Duhamel, Phys. Lett. **57B**, 338 (1975).
[13] H. Langevin-Joliot, E. Gerlic, J. Guillot, M. Sakai, J. Van de Wiele, A. Devaux, P. Force, and G. Landaud, Phys. Lett. **114B**, 103 (1982).
[14] H. Langevin-Joliot, J. Van de Wiele, J. Guillot, E. Gerlic, L. H. Rosier, A. Willis, M. Morlet, G. Duhamel-Chretien, E. Tomasi-Gustafsson, N. Blasi, S. Micheletti, and S. Y. van der Werf, Phys. Rev. C **47**, 1571 (1993).
[15] J. Van de Wiele, H. Langevin-Joliot, J. Guillot, L. H. Rosier, A. Willis, M. Morlet, G. Duhamel-Chrétien, E. Gerlic, E. Tomasi-Gustafsson, N. Blasi, S. Micheletti, and S. Y. van der Werf, Phys. Rev. C **46**, 1863 (1992).
[16] J. Van de Wiele, H. Langevin-Joliot, F. Jourdan, J. Guillot, E. Gerlic, L. H. Rosier, A. Willis, C. Djalali, M. Morlet, E. Tomasi-Gustafsson, N. Blasi, S. Micheletti, and S. Y. van der Werf, Phys. Rev. C **50**, 2935 (1994).
[17] J. Van de Wiele, A. I. Vdovin, and H. Langevin-Joliot, Nucl. Phys. **A605**, 173 (1996).
[18] J. Arvieux, S. D. Baker, A. Boudard, J. Cameron, T. Hasegawa, D. Hutcheon, C. Kerboul, G. Gaillard, and Nguyen Van Sen, Nucl. Instrum. Methods Phys. Res. A **273**, 48 (1988).
[19] B. Bonin, A. Boudard, H. Fanet, R. W. Fergerson, M. Garçon, C. Giorgetti, J. Habault, J. Le Meur, R. M. Lombard, J. C. Lugol, B. Mayer, J. P. Mouly, E. Tomasi-Gustafsson, J. C. Duchazeaubeneix, J. Yonnet, M. Morlet, J. Van de Wiele, A. Willis, G. Greeniaus, G. Gaillard, P. Markowitz, C. F. Perdrisat, R. Abegg, and D. A. Hutcheon, Nucl. Instrum. Methods Phys. Res. A **288**, 379 (1990).
[20] H. Quechon, Thesis, Orsay, 1980; J. Radin, H. Quechon, G. M. Raisbeck, and F. Yiou, Phys. Rev. C **26**, 2565 (1982).
[21] A. Van der Woude, Prog. Part. Nucl. Phys. **18**, 217 (1987).
[22] M. J. Martin, Nucl. Data Sheets **47**, 797 (1986).
[23] D. H. Youngblood, J. M. Moss, C. M. Rozsa, J. D. Bronson, A. D. Bacher, and D. R. Brown, Phys. Rev. C **13**, 994 (1976).
[24] Y. Fujita, M. Fujiwara, S. Morinobu, I. Katayama, T. Yamasaki, T. Itahashi, and H. Ikegami, Phys. Rev. C **32**, 425 (1985).
[25] M. Beiner, H. Flocard, and Nguyen Van Giai, Nucl. Phys. **A238**, 29 (1975).
[26] J. Van de Wiele, computer code CCZR, Institut de Physique nucléaire, Orsay, IN2P3-CNRS (unpublished).
[27] N. Austern, Nucl. Phys. **A292**, 190 (1977).
[28] P. D. Kunz, computer code DWUCK5, University of Colorado.
[29] J. L. Ballot, J. Van de Wiele, and G. Cory (unpublished); J. Van de Wiele, IPN-DRE Orsay Annual Report, p. 78, 1989.
[30] R. De Tourreil and D. W. Sprung, Nucl. Phys. **A201**, 193 (1973).
[31] G. F. Bertsch, P. F. Bortignon, and R. A. Broglia, Rev. Mod. Phys. **55**, 287 (1983).
[32] M. Waroquier (private communication).
[33] D. Van Neck, M. Waroquier, and J. Ryckebush, Nucl. Phys. **A563**, 1 (1993).
[34] D. Van Neck, M. Waroquier, and J. Ryckebush, Nucl. Phys. **A530**, 347 (1991).
[35] J. W. A. den Herder, H. P. Blok, E. Jans, P. K. M. Keizer, L. Lapikàs, E. N. M. Quint, G. van der Steenhoven, and P. K. A. de Witt Huberts, Nucl. Phys. **A490**, 507 (1988).